A micromagnetic study of surface-acoustic-wave-driven excitation of spin waves in an iron-based conduit

I. Ngouagnia Yemeli, L. Christienne, P. Rovillain, J.-Y. Duquesne, A. Anane, M. Marangolo, Daniel Stoeffler

A micromagnetic study of Surface-Acoustic-Wave-Driven Excitation of Spin Waves in an Iron-based Conduit:

I. Ngouagnia Yemeli,[1, a)] L. Christienne,[2] P. Rovillain,[2] J.-Y. Duquesne,[2] A. Anane,[3] M. Marangolo,[2] and D. Stoeffler[1]

[1)]*Université de Strasbourg, CNRS, Institut de Physique et Chimie des Matériaux de Strasbourg, UMR 7504, France*

[2)]*Sorbonne Université, CNRS, Institut des NanoSciences de Paris, INSP, F-75005 Paris, France*

[3)]*Laboratoire Albert Fert, CNRS, Thales, Université Paris-Saclay, 91767 Palaiseau, France*

(Dated: 25 March 2025)

We propose a magnonic device based on resonant magnetoelastic coupling and surface acoustic waves as an alternative way to excite spin waves. Using micromagnetic simulations, we study the generation and propagation of spin waves in an FeN waveguide from the excitation of an inserted Fe pad using surface acoustic waves. First, we derive the approximate but reliable expression for the effective magnetoelastic field taking into account the magnetorotative contribution and the geometry of the system. Second, we show that a propagating spin wave generated from the Fe pad is obtained with an attenuation length around 2 μm. By studying the behaviour of the spin wave in the conduit as a function of the external field and the surface acoustic wave frequency, we deduce the optimal working conditions for the system. Interestingly, an asymmetric propagation of spin waves in the conduit is clearly anticipated by simulations.

I. INTRODUCTION

Magnonics plans to use spin waves (SWs), *i.e.* the collective precessional motion of spins in magnetic media, to process information[1,2]. With frequencies in the GHz-THz range and wavelengths in the micron and submicron range, they are of great interest for applications in microlectronics, information and telecommunication technologies[3]. Over the last decade, some basic building blocks of the magnonic paradigm have been experimentally demonstrated such as the magnon-transistor[4], the magnonic majority-gate[5], the spin-torque-induced amplification of SWs[6] and the magnonic diode[7]. However, up to now, those building blocks intrinsically consume much more energy than their CMOS counterparts as they still rely on Œrsted fields for signal transduction. Here, we propose an innovative approach based on elastic strain to overcome this issue, allowing large scale integration of voltage controlled magnonic circuits. Indeed, under the effect of strain, a magnetic material can undergo a change in its magnetic susceptibility, referred to as the magnetoelastic effect. Taking advantage of this resonant MagnetoElastic Coupling (MEC), Surface Acoustic Waves (SAWs) can be used to excite magnetization dynamics, *i.e.* SAW induced Ferromagnetic Resonance (SAW-FMR)[8–12]and consequent SWs propagation through an adjacent waveguide[13,14].

In this work, the traditional inductive antennas found in magnonic devices are replaced by SAW-induced SW emission, avoiding Joule energy dissipation. Remote SAW transducers activate local magnetoelastic micro-resonators (the Fe pad in Figure 1) which, in turn, inject traveling SWs into waveguides slightly responsive to traveling SAW (the FeN conduit of Figure 1).

In the device presented in Figure 1, SAW-FMR is obtained in a Fe mesa grown on a piezoelectric GaAs. Note that in addition to this MEC effect, which is associated with an effective MEC field $\boldsymbol{H}^{ME}$, there is also a magnetorotation coupling that describes the rotational deformation of the lattice at the surface, where lattice points rotate with the SAW-imposed chirality, modifying the magnetic anisotropy and yielding an effective magnetorotation coupling field[15,16] $\boldsymbol{H}^{MR}$ dependent on the magnetization, $\boldsymbol{M}$, and the crystalline anisotropy.

Rayleigh waves are described by the following displacement vector (the $\boldsymbol{X}$-axis parallel to the [110] direction):

$$\boldsymbol{u}(X,Z,t) = \begin{pmatrix} u_X(Z)\cos(k_{SAW}X - \omega t) \\ 0 \\ u_Z(Z)\sin(k_{SAW}X - \omega t) \end{pmatrix} \qquad (1)$$

as schematically shown in Figure 1. It is necessary to make the FeN conduit operate out of SAW-FMR. In this work, we achieve this by slightly modifying the SW spectrum through the implantation of nitrogen atoms into the pristine Fe structure (hence the designation FeN conduit). We have indeed already demonstrated that such implantation leads to a high level of tunability of the Fe film magnetic anisotropy, which will then allow the desired control on the SW dispersion[17,18]. This operation will allow the Fe pad to be excited with SAW-FMR while the adjacent FeN conduit operates out of SAW-FMR.

II. SYSTEM DESCRIPTION

Figure 1 shows a schematic of the typical device used in this study. It consists of an interdigital transducer (IDT) and a magnetic material waveguide, on top of a piezoelectric substrate, GaAs(001), with the following epitaxial conditions : Fe[100]//GaAs[100] and Fe(001)//GaAs(001). The magnetic material waveguide is an FeN conduit (an Fe conduit where N atoms have been implanted) with an Fe pad at its centre, *i.e.* a FeN-Fe-FeN configuration. In the experiment, when excited

[a)]Corresponding author : igorngouagnia@yahoo.fr

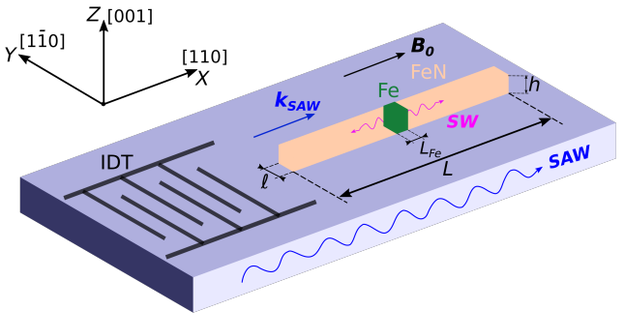

FIG. 1. (Color online). Envisioned experimental set-up used to excite spin waves in the FeN conduit. Spin waves are generated through the resonant excitation of magnetization precession in the Fe pad, driven by surface acoustic waves.

by an rf voltage, the IDT emits SAWs, which propagate towards the magnetic material, along the Fe magnetic hard axis (*i.e.* the [110] direction), with a wavevector $\boldsymbol{k}_{SAW}$. An external magnetic field $\boldsymbol{B}_0$ is applied along the SAW propagation direction. Then, SAWs are expected to excite the magnetization of the Fe pad due to MEC, which in turn generates magnon excitations that propagate in the conduit. Nitrogen implantation alters the magnetic properties of the conduit, shifting it out of the SAW-FMR, *i.e.* reducing the local SW's excitation by SAW.

The conduit is L = 30 μm long, ℓ = 1 μm wide and h = 53 nm thick. In our micromagnetic simulations, we consider infinitely long conduits by applying periodic boundary conditions (PBC) in the $\boldsymbol{X}$ direction on a 30 μm long unit cell. The Fe pad is L_{Fe} = 4 μm long. The system is discretized using a rectangular mesh $N_X \times N_Y \times N_Z$. The dimensions of a cell are $h_X = L/N_X$, $h_Y = \ell/N_Y$, $h_Z = h/N_Z$. Initially, we used the discretization 10000 × 300 × 16 for which the unit cell dimensions (h_X = 3 nm, h_Y = 3.33 nm, h_Z = 3.31 nm) are equal to the exchange length Λ_{ex} = 3.3 nm, in order to accurately take into account the exchange interaction in the calculation. Then, using the discretization 5000 × 150 × 8, we obtained similar results. We therefore adopted it for all calculations.

The magnetic parameters of Fe and FeN are given in Appendix A. These values are reliable as they were obtained experimentally from N implanted Fe thin films. The main difference is in the strentgh of the anisotropy. The Perpendicular Magnetic Anistropy (PMA) is K_u = 150 kJ/m^3 for FeN and K_u = 100 kJ/m^3 for Fe, due to nitrogen implantation. More important, the cubic anisotropy is slightly smaller for FeN as compared to the Fe one : K_{c1}(FeN) = 40 kJ/m^3 and K_{c1}(Fe) = 49.6 kJ/m^3. The static field B_0 = 34 mT (above the saturation field of the conduit) is applied along the hard axis [110] (the $\boldsymbol{X}$-axis of the reference frame (XYZ) - see Figure 1), which is chosen as the SW's propagation vector (backward configuration) in order to get a SW's softening and a resonant matching with SAW frequency in the Fe pad[19]. In the following, we simulate the propagation of SWs through the FeN conduit. These SWs are generated by the magnetization dynamics of the Fe pad, activated resonantly by traveling SAWs.

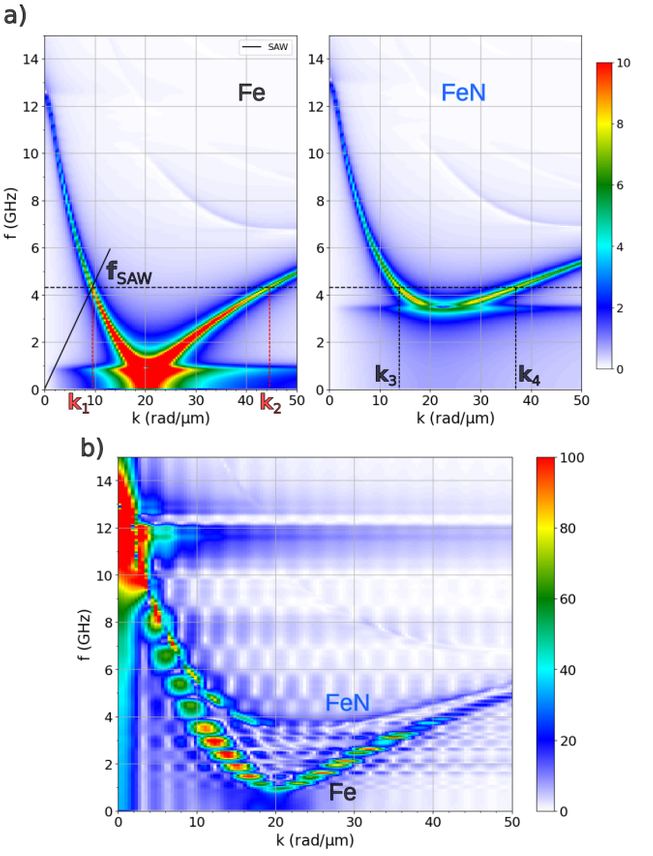

FIG. 2. (Color online). a) Dispersion curves for two infinite conduits of Fe and FeN calculated using Periodic Boundary Conditions (PBC). The black line is the numerically calculated SAW dispersion, which is linear until 6 GHz. b) Dispersion curve of the real system with an Fe pad of length L_{Fe} = 4 μm at the center of the 30 μm length FeN conduit. These simulations are done at B_0 = 34 mT.

III. MAGNETOELASTIC AND MAGNETOROTATION EFFECTIVE FIELD - MUMAX3

For micromagnetic simulations, we use MuMax3 which is a GPU-accelerated micromagnetic simulation program which solves the time- and space dependent magnetization evolution in nano- to micro scale magnets using a finite-difference discretization[20]. To describe the interaction between SAWs and the magnetization vector, we begin by examining the magnetoelastic and magnetorotational free energy in a cubic solid. In the standard implementation of MuMax3, the magnetoelastic field $\boldsymbol{H}^{ME}$ is defined within the (xyz) coordinate framework, where x//[100]. Consequently, the field reads as follows :

$$\boldsymbol{H}^{ME}(x,y,z) = -\frac{2}{\mu_0 M_s}\begin{pmatrix} B_1 m_x \varepsilon_{xx} + B_2(m_y\varepsilon_{xy} + m_z\varepsilon_{xz}) \\ B_1 m_y \varepsilon_{yy} + B_2(m_x\varepsilon_{yx} + m_z\varepsilon_{yz}) \\ B_1 m_z \varepsilon_{zz} + B_2(m_x\varepsilon_{zx} + m_y\varepsilon_{zy}) \end{pmatrix} \quad (2)$$

where m_i ($i = x,y,z$) are the magnetization components, ε_{ij}

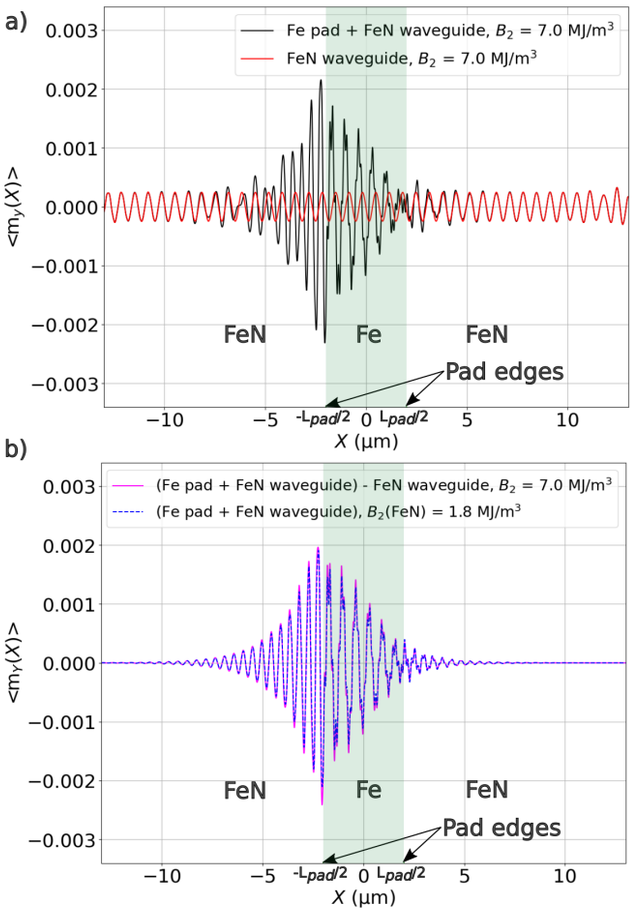

FIG. 3. (Color online). a) Profile of the transverse magnetization $\langle m_Y(X, 100 \times T)\rangle$ within the infinite FeN conduit with Fe pad (black curve) and the FeN conduit alone (red curve) after excitation of the conduit by a surface acoustic wave at f_{SAW} = 4.32 GHz and k_{SAW} = k_1 = 9.46 rad/μm for B_0 = 34 mT. The simulations are performed using the same magnetoelastic constant for Fe and FeN, B_2 = 7.0 MJ.m^{-3}. b) Difference between the 2 signals in figure a) (magenta curve) and simulation result for the infinite FeN conduit with Fe pad using B_2(FeN) = $\mu_0 M_S^2/2$ = 1.8 MJ.m^{-3} (dashed blue curve). In a) and b), the region of the Fe pad is shown with the green transparent rectangle. The pad edges are also indicated.

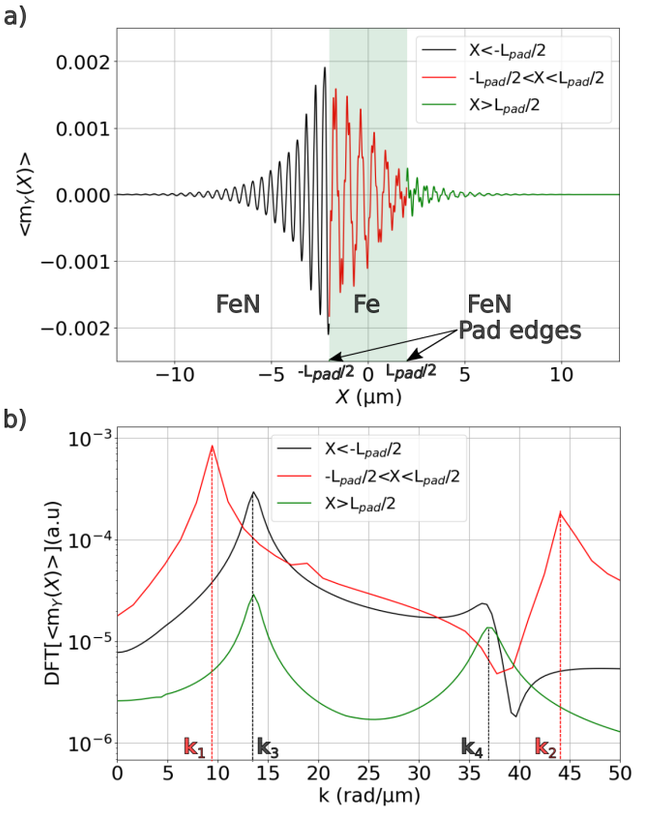

FIG. 4. (Color online). a) Representation of the spin wave profile generated in the conduit, highlighting the 3 different parts FeN-Fe-FeN with different colors. The region of the Fe pad is shown with the green transparent rectangle. The pad edges are also indicated. b) Signals obtained by discrete Fourier transform (DFT) of the different curves in figure a) with the corresponding colors.

$(i, j = x, y, z)$ are the components of the strain tensor expressed in the standard cubic frame (x//[100], y//[010], z//[001]), and B_1 and B_2 the magnetoelastic coupling constants. In order to describe Rayleigh waves propagation it is important to recall that the strain tensor ε and the rotation tensor ω are defined as follows[21]:

$$\begin{cases} \varepsilon_{ij} = \dfrac{1}{2}\left(\dfrac{\partial u_i}{\partial x_j} + \dfrac{\partial u_j}{\partial x_i}\right) \\ \omega_{ij} = \dfrac{1}{2}\left(\dfrac{\partial u_i}{\partial x_j} - \dfrac{\partial u_j}{\partial x_i}\right) \end{cases} \tag{3}$$

As stated in the introduction, the rotation of lattice points induces an effective magnetorotation field, $\boldsymbol{H}^{MR}$. Interestingly, this field can rotate either in the same direction as the magnetization vector or in the opposite direction. This dynamic interplay leads to a significant nonreciprocal coupling between SAWs and SWs, as reported in reference[15]. When the out-of-plane magnetocrystalline anisotropy energy ($K_u \approx$ 100 kJ.m^{-3} in our case) is significantly lower than the demagnetizing energy ($\mu_0 M_s^2/2 \approx$ 1800 kJ.m^{-3} in Fe thin films) and thus negligible, the energy density simplifies to :

$$f_{rot} = \mu_0 M_s^2(\omega_{yz} m_y m_z + \omega_{xz} m_x m_z) \tag{4}$$

The corresponding magnetorotation effective field $\boldsymbol{H}^{MR}$ is given by $\boldsymbol{H}^{MR}(x,y,z) = -\frac{1}{\mu_0}\frac{\partial f_{rot}}{\partial \boldsymbol{M}}$ which yields :

$$\boldsymbol{H}^{MR}(x,y,z) = -M_s \begin{pmatrix} \omega_{xz} m_z \\ \omega_{yz} m_z \\ \omega_{yz} m_y + \omega_{xz} m_x \end{pmatrix} \tag{5}$$

As mentioned in the introduction, we are interested in SAWs and SWs propagation along the hard axis of Fe, *i.e.* the [110] axis. Thus, we consider the rotated frame (X//[110], Y//[1$\bar{1}$0], Z//[001]) which makes an angle of 45° with (xyz),

see Figure 10 in Appendix C. We had already used these two frames, the standard cubic frame and the rotated frame, in our two previous studies[19,22]. To facilitate MuMax3 simulations, we use a rough approximation according to which the SAW profile does not depend on the film thickness Z, that is much smaller than the SAW wavelength. So, in equation 1 we consider that u_X and u_Z are constants of values u_{0X} and u_{0Z}[23]. The total magnetoelastic and magnetorotation effective field can be expressed as follows (the calculations are given in Appendix C) :

$$\boldsymbol{H}^{ME-MR}(X,Y,Z) = -\frac{2}{\mu_0 M_S}\begin{pmatrix} \frac{B_1+B_2}{2} m_X \varepsilon_{XX} + (B_2 - \frac{\mu_0 M_S^2}{2}) m_Z \varepsilon_{XZ} \\ \frac{B_1-B_2}{2} m_Y \varepsilon_{XX} \\ (B_2 - \frac{\mu_0 M_S^2}{2}) m_X \varepsilon_{XZ} \end{pmatrix} \tag{6}$$

where $\varepsilon_{XX} = \frac{\partial u_X}{\partial X}$, $\varepsilon_{XZ} = \frac{1}{2}\frac{\partial u_Z}{\partial X}$. For a displacement of the form $\boldsymbol{u}(X,t) = (u_{0X}\cos(k_{SAW}X - \omega t), 0, u_{0Z}\sin(k_{SAW}X - \omega t))$ at a frequency f_{SAW}, one finds that $\varepsilon_{XX} = \varepsilon_{XX0}\sin(k_{SAW}X - \omega t)$ and $\varepsilon_{XZ} = \varepsilon_{XZ0}\cos(k_{SAW}X - \omega t)$, where $\varepsilon_{XX0} = -k_{SAW}.u_{0X}$ and $\varepsilon_{XZ0} = \frac{1}{2}k_{SAW}.u_{0Z}$ are the amplitudes of ε_{XX} and ε_{XZ} respectively. Similarly, the only non-zero component of the rotation tensor is $\omega_{XZ} = -\varepsilon_{XZ}$. The following simulation results were obtained for $u_{0X} = u_{0Z} = u_0 = 1\text{pm} = 10^{-12}\text{m}$. In the case f_{SAW} = 4.32 GHz, k_{SAW} = 9.46 rad/μm, which leads to typical amplitudes of the components of the strain tensor $\varepsilon_{XX0} = -9.46\times10^{-6}$ and $\varepsilon_{XZ0} = 4.73\times10^{-6}$.

IV. SPIN WAVE CHARACTERISTICS FOR SATURATED MAGNETIZATION

The saturation field of the FeN conduit is 22 mT. Therefore, for an applied static field B_0 = 34 mT, the conduit is initially saturated, so that the normalized equilibrium magnetization is $\boldsymbol{m}$ = (m_X,m_Y,m_Z) = (1,0,0). As a result, equation 6 can be reformulated as follows :

$$\boldsymbol{H}^{ME-MR}(X,Y,Z) = -\frac{2}{\mu_0 M_S}\begin{pmatrix} \frac{B_1+B_2}{2}\varepsilon_{XX} \\ 0 \\ (B_2 - \frac{\mu_0 M_S^2}{2})\varepsilon_{XZ} \end{pmatrix} \tag{7}$$

In this case, only the X and Z components of $\boldsymbol{H}^{ME-MR}$ are non-zero. So, since magnetization is along the $\boldsymbol{X}$-axis, only the Z component of $\boldsymbol{H}^{ME-MR}$ can excite the magnetization. Therefore, the only MEC constant affecting the dynamics is B_2. For this reason, only this constant is used in the simulations, B_1 = 0.

Figure 2.a presents the dispersion curves for two infinite conduits of Fe and FeN in the so-called backward configuration, which is characterized by a negative group velocity at low k-values, given by the slope of the tangent to the dispersion curve. To access these dispersion curves, a strong 5 mT pulse is applied over the two central cells planes of the grid ($-h_X < X < +h_X$) during 10 ps, and then the transverse magnetization $m_Y(X,t)$, averaged over each (YZ) section along the $\boldsymbol{X}$-axis is recorded for 20 ns. The dispersion curves are obtained by performing a double (in space and time) Discrete Fourier Transform (DFT) of this spatio-temporal signal. The numerically calculated SAW dispersion curve which is linear until 6 GHz, is shown by the straight black line on the Fe dispersion curve in Figure 2.a. Figure 2.b shows the dispersion curve of the real system where the short pulse is now applied on the Fe pad inside the FeN conduit. It is similar to a combination of the dispersion curves for infinite conduits with high amplitude hot spots and almost zero amplitude points due to the finite size of the excitation.

The SAW is then applied at the matching point corresponding to the intersection of the Fe and SAW dispersion curves : f_{SAW} = 4.32 GHz and k_{SAW} = 9.46 rad/μm for B_0 = 34 mT. In these simulations, neither linewidth broadening due to backaction effects nor the anticrossing regime are taken into account[24]. Indeed, in our previous studies[19,22], only slight variations in the relative velocity, on the order of 10^{-4}, were observed, dependent on the intensity of the magnetic field. We did not observe SAW propagation affected by an anticrossing regime under SAW-FMR conditions, i.e. SAW propagating from the IDT source to the IDT receiver, 4 mm away, even at resonance. Achieving such a regime would require either strong MEC and a long SW lifetime, ensuring significant magnon-phonon overlap (as in YIG), or the use of an acoustic cavity, as demonstrated by Hwang et al. in reference[25].

At this matching point, the group velocity is negative. The simulations are performed using the same magnetoelastic constant B_2 = 7 MJ/m^3 for Fe and FeN[19]. The Landau–Lifshitz–Gilbert equation is first solved for 100 periods $T = 1/f_{SAW}$ to ensure that steady state is reached and the transverse magnetization $m_Y(X, 100\times T)$ taken at $t = 100\times T$, averaged over each (YZ) section perpendicular to the $\boldsymbol{X}$-axis ($\langle m_Y(X, 100\times T)\rangle$) is analyzed. Figure 3.a shows the profile of $\langle m_Y(X, 100\times T)\rangle$ in two cases, the one of the system studied, Fe pad in FeN conduit (black curve) and the one of an FeN conduit alone (without Fe pad) of the same geometry (red curve). The pad is shown by the green transparent rectangle. The red curve is a sinusoidal signal of constant amplitude, corresponding to direct excitation of the conduit by the SAW despite being outside SAW-FMR conditions. This signal must be minimized to ensure practical applicability in real-world devices.

Analyzing the induced SWs within the FeN conduit provides valuable insights and understanding. Indeed, we can notice that the signal amplitude peaks (black curve) at the pad edge at -$L_{pad}/2$ and decreases on either side of this edge, until it almost cancels out at +$L_{pad}/2$. Outside the area [- 6 μm, 2 μm], its amplitude remains almost constant in the rest of the conduit, coinciding with the red signal. These results indicate that there is a superposition in the FeN conduit of direct excitation by the SAW and excitation of SWs from the adjacent Fe pad. The contribution from the Fe pad alone is deduced by a difference between the two signals. This is shown in the magenta curve in Figure 3.b. Propagation is different on both sides of the pad : the signal amplitude is maximal at the $-L_{pad}/2$ edge, but decreases until it virtually cancels out at the $+L_{pad}/2$ edge. This induces a clear difference between

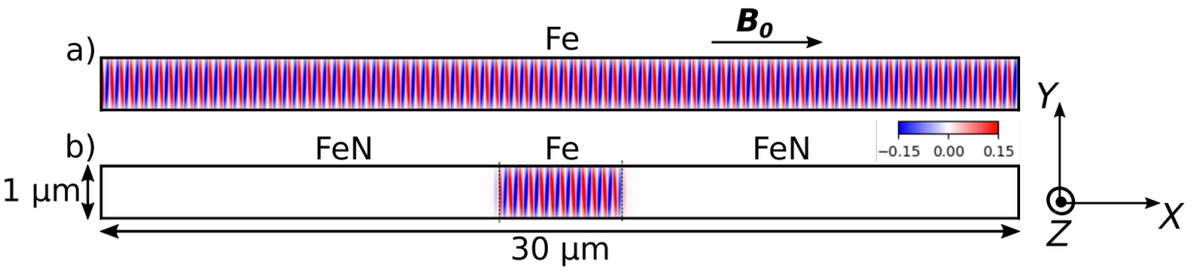

FIG. 5. (Color online). a) Equilibrium transverse magnetization profile m_Y in the mid-plane $Z = h/2$ of the infinite Fe conduit, for B_0 = 30 mT. b) Equilibrium transverse magnetization profile m_Y in the mid-plane $Z = h/2$ of the infinite FeN conduit with Fe pad, for B_0 = 30 mT. The edges of the conduit and the pad are shown for better visualization.

TABLE I. Characteristics at different f_{SAW} at B_0 = 34 mT.

f_{SAW}(GHz)	k_a(rad/µm)	A_a ($\times 10^{-3}$)	L_{att-a} (µm)	k_b(rad/µm)	A_b ($\times 10^{-3}$)	L_{att-b} (µm)
4.22	14.0	2.45	1.5	35.8	0.42	0.85
4.32	13.6	2.4	1.6	37.0	0.32	0.88
4.42	13.2	1.87	1.7	38.2	0.21	0.91

the two FeN areas on either side of the pad, *i.e.* the propagation of SWs is enhanced in the direction opposite to that of the SAWs. In other words, the SAW-FMR effect in the Fe pad induces an asymmetric excitation within the FeN conduit. Despite the difference in amplitude, the propagation of SWs follows an exponential trend in both directions, as expected for SWs generated.

When the direction of SAW propagation is changed, the signal is inversed by central symmetry with respect to the center of the conduit, see Figure 9 in Appendix B. We have also found that reversing the direction of the magnetic field has no effect on the signal obtained (even if, of course, the direction of rotation of the magnetization is reversed): the signal remains exactly the same. The inversion by central symmetry observed when the direction of SAW propagation is reversed is simply due to the change in the direction of propagation of the excitation that is the SAW here. So the system does not exhibit non-reciprocity.

To isolate the propagation of SWs in the FeN conduit, induced by the neighboring Fe pad, from the local magnetization dynamics excited by the traveling SAW, we introduce a carefully selected B_2 value. This specific $B_2 = \mu_0 M_s^2/2$ = 1.8 MJ/m^3 ensures the cancellation of direct SAW excitation of the FeN conduit magnetization. Indeed, it appears in equation 7 that $B_2 = \mu_0 M_s^2/2$ cancels out the Z component. The magnetoelastic and magnetorotation field is thus reduced to its X component, parallel to the magnetization, which explains why the FeN conduit is insensitive to the SAW in this case. With this B_2 value, the obtained SWs excitation is shown in Figure 3.b (dashed blue curve). We observe that the SW excitation obtained using the specific *ad hoc* B_2 value (B_2 = 1.8 MJ/m^3) aligns closely with the results from the subtraction procedure discussed earlier (magenta curve in Figure 3.b). This consistency confirms that the signal in the conduit comprises both the local excitation induced by the SAW with B_2 = 7 MJ/m^3 and the SWs injected by the neighboring Fe pad.

To determine the excited modes in the conduit, we perform a DFT of the signal in Figure 3.b. Figure 4 shows the result obtained. Figure 4.a shows the signal from Figure 3.b, divided into 3 parts corresponding to the Fe pad (red portion) and both sides of the FeN conduit (black and green portions). The three curves in Figure 4.b are obtained by spatial DFT of these three parts, using the corresponding colors. The red curve shows that the main mode excited in the Fe pad at f_{SAW} = 4.32 GHz is $k_1 = 9.46\ rad/\mu\text{m} = k_{SAW}$, as expected from the Fe dispersion curve in Figure 2.a. The second resonance mode of the Fe pad at k_2 = 44.5 rad/μm is also excited but out of resonance, which explains why its amplitude is much smaller. The black and green curves show that two modes are excited in the conduit, at k_3 = 13.6 rad/μm and k_4 = 37.0 rad/μm, as expected from the FeN dispersion curve in Figure 2.a. The amplitudes of those modes are higher in the left-hand side of the conduit (black curve) than in the right-hand side (green curve), in agreement with the signal in Figure 4.a.

Varying f_{SAW} around 4.32 GHz confirms that this frequency can be considered as the system's working point where the SW induced by the excitation of the Fe pad has the largest amplitude. This is done by fitting the $\langle m_Y(X, 100 \times T)\rangle$ curve with the usual expression $m_Y(X) = A_a e^{-X/L_{att-a}} \cos(k_a X + \varphi_a) + A_b e^{-X/L_{att-b}} \cos(k_b X + \varphi_b)$ to get the amplitude A_i and the attenuation length L_{att-i} for each wave vector k_i, where i = a,b. Table I shows the results of such a fit for a variation of ± 0.1 GHz. The curves are shown in Figure 11.a in the appendix D for the part of the signal at the left of the pad ($X < -L_{pad}/2$). For 4.32 GHz, one finds without surprise the wave vectors k_3 and k_4 of Figure 4.b. The attenuation length of the highest amplitude mode is 1.6 µm. The same analysis was done for the signal in the positive part, see Figure 11.b in appendix D. The wave vectors and attenuation lengths are exactly the same, which means that it is intrinsically the same SW modes that propagate on both sides of the pad, only the amplitudes are different. This difference in am-

plitude highlights the asymmetric propagation of SWs within the FeN conduit shown in Figure 4.a.

Here, we propose a hypothesis to explain the mechanism underlying the observed asymmetric behavior. Suppose the SAW propagates through the Fe mesa from left to right, with $k_{SAW} = k_1$. The primary excitation (energy transfer) in the FeN conduit occurs at the nearest matching wave vector, as shown in Figure 4.b, i.e. k_3. We observe that the SW group velocity at k_3 is negative, as indicated in Figure 2.b. Consequently, energy transfer from the Fe pad efficiently excites SWs in the left part of the conduit, with these waves propagating toward the left. In contrast, SWs in the right part of the conduit cannot be excited effectively.

This simplified description captures the essential physics of the asymmetric SW generation observed in our simulations. However, a more in-depth analysis of SW excitation mechanisms is required and will be presented in a future article.

V. CASE STUDY ON MAGNETIC DOMAIN STRUCTURED FE PAD

So far, this work has been carried out at a static field of 34 mT, above the saturation field of the Fe pad and of the FeN conduit. It is interesting to see what happens below this critical field. Figure 5 shows the profile of the magnetization component m_Y in the mid-plane $Z = h/2$ at equilibrium at B_0 = 30 mT, in two cases, for the Fe conduit in Figure 5.a and for the FeN conduit with Fe pad in Figure 5.b. Both the Fe conduit and the Fe pad within the FeN conduit are structured, with alternating magnetic domains with opposite transverse magnetization of amplitude 0.15.

It is insightful to compare the SW dispersion curves of two infinite Fe and FeN conduits under a saturating field of 34 mT (Figure 2.b) with those reported in Figure 6.a calculated at 30 mT. The vertical line on the Fe curve at k = 20 rad/μm in Figure 6.a is an artefact of the DFT calculation, this wave vector value corresponding to the period of the Fe conduit structuration in Figure 5.a.

For FeN, there is mainly a frequency downshift in the dispersion curve. For Fe, the shape of the curve changes, with the emergence of several branches that are reminiscent of those of a magnonic crystal, a medium whose magnetic properties are characterized by periodic variation in space[26]. The two intersection points of maximum amplitude with the SAW dispersion curve are indicated on Figure 6.a, f_1 = 3.215 GHz and f_2 = 4.1 GHz. As before, we calculated the $m_Y(X, 100 \times T)$ signal at various frequencies, ranging from below f_1 to above f_2. Figure 6.b shows the corresponding curves obtained after spatial DFT. The working point is not directly predictable from the dispersion curve; we notice that the optimal frequency where the main mode is excited with maximum amplitude is rather f = 3.8 GHz, an intermediate value between f_1 and f_2.

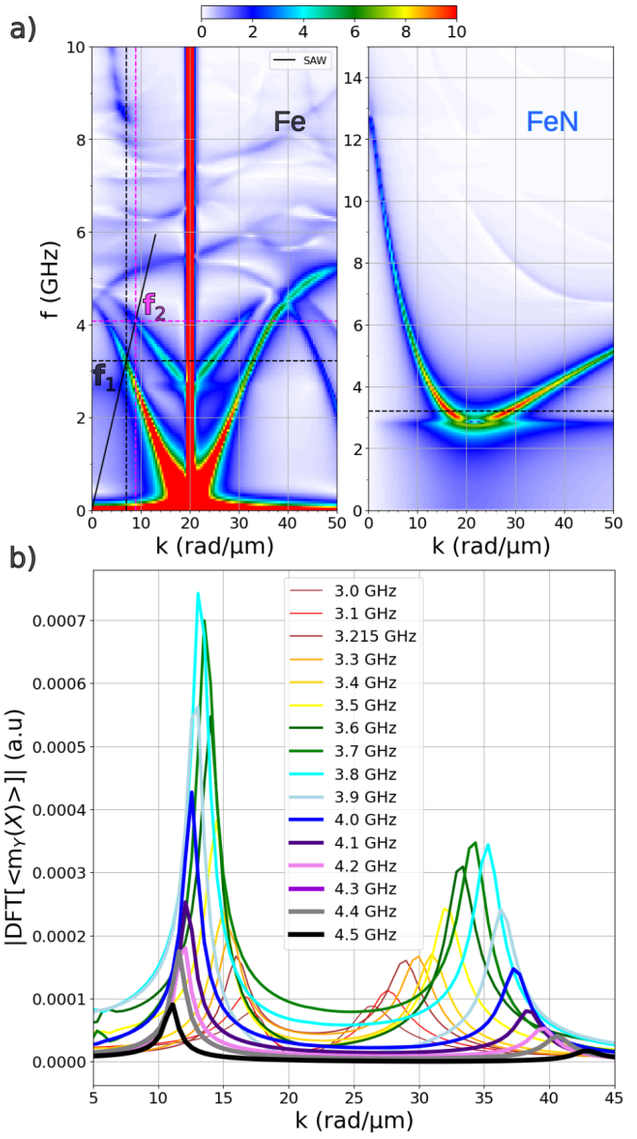

FIG. 6. (Color online). a) Dispersion curves for two infinite conduits of Fe and FeN calculated using PBC at B_0 = 30 mT. The solid black line is the SAW dispersion. The intersection frequencies of the Fe and SAW dispersions are labeled f_1 and f_2. b) Signals obtained by DFT of the spin wave profile generated in the FeN conduit at different f_{SAW} swept between f_1 and f_2.

VI. OPTIMIZING SAW-DRIVEN SPIN WAVE EXCITATION AND PROPAGATION IN FEN CONDUITS

To optimize the SAW-driven excitation of SWs in the FeN conduit, it is essential to identify the optimal combination of SAW excitation frequency and external magnetic field (f_{SAW}, B_0) that satisfies two requirements. First, enhance genuine SW excitation, *i.e.* maximize the excitation of true SWs relative to the SAW-induced magnetization dynamics within the conduit. Second, maximize SW attenuation length, *i.e.* achieve the greatest possible propagation distance for the SWs

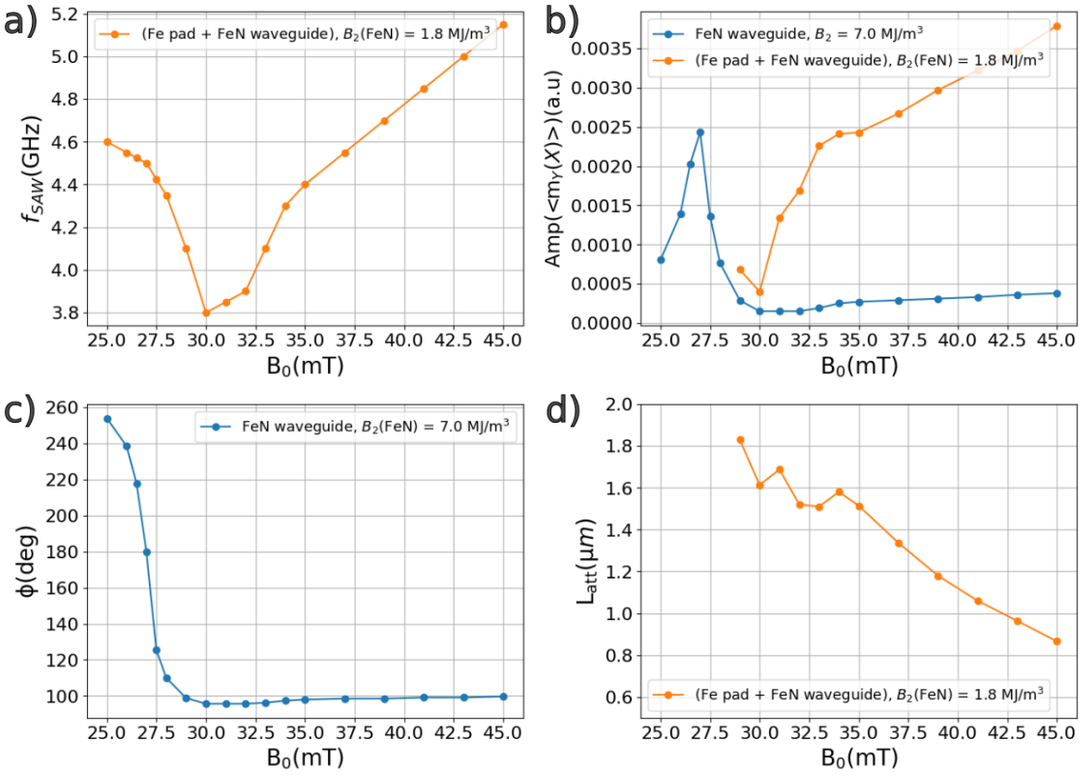

FIG. 7. (Color online). a) Magnetic field dependence of the SAW frequency f_{SAW} at which the system response (FeN conduit with Fe pad) is maximum. b) Amplitude of the transverse magnetization $\langle m_Y(X, 100 \times T)\rangle$ as a function of the magnetic field in the case of an FeN conduit alone (blue curve) and a conduit with Fe pad (orange curve), the conduit being excited at each field at the corresponding frequency f_{SAW} shown in a). c) Phase of the transverse magnetization $\langle m_Y(X, 100 \times T)\rangle$ relative to the SAW as a function of magnetic field in the case of the FeN conduit alone. d) Magnetic field dependence of the attenuation length of the spin wave generated in the conduit.

before significant attenuation occurs.

Enhancing genuine SW excitation : in the following, we identify the conditions that maximize the contrast between SWs injected by the Fe pad and the excitations induced by the SAW propagating through the FeN conduit (as done for results reported in Figure 3). The SAW-induced excitations are calculated for an infinite FeN conduit with B_2 = 7 MJ/m^3, while the injected SWs are evaluated in the FeN-Fe-FeN system with B_2(FeN) = 1.8 MJ/m^3. The (f_{SAW}, B_0) values are determined by locating the intersection point between the Fe conduit dispersion curve at B_0 and the linear SAW dispersion curve. For fields $<$ 34 mT where there are several points of intersection, we consider the one where excitation in the conduit is of maximum amplitude, for example f_{SAW} = 3.8 GHz at B_0 = 30 mT from the results in Figure 6.b.

A plot illustrating the resulting (f_{SAW}, B_0) dependence is shown in Figure 7.a. First, for each (f_{SAW}, B_0) value, the SAW-induced magnetization dynamics are evaluated in the infinite FeN conduit with B_2 = 7 MJ/m^3. The signal $\langle m_Y(X, 100 \times T)\rangle$ reflects the SAW excitation, i.e. a sinusoidal signal with wave vector $k = k_{SAW}$. A fit of this signal with a formula $A\cos(k_{SAW}X + 2\pi f_{SAW}t + \phi)$ allows to deduce the amplitude A of the signal and the phase shift ϕ with the SAW. The blue curves of Figures 7.b & c show the results obtained. These curves highlight the resonance of the SW induced in the FeN conduit by SAW at B_0 = 27 mT. Above 30 mT, the SAW-induced magnetization dynamics are significantly reduced, as shown in Figure 7.b. The same figure also illustrates that pure SWs (calculated with B_2(FeN) = 1.8 MJ/m^3 in FeN-Fe-FeN) are reinforced as the magnetic field increases. Relevant parameters are obtained by fitting the signal with the expression $m_Y(X) = A_a e^{-X/L_{att-a}}\cos(k_a X + \varphi_a) + A_b e^{-X/L_{att-b}}\cos(k_b X + \varphi_b)$, where L_{att-a} and L_{att-b} are the attenuation lengths.

Maximize SW attenuation length : in the following, we identify the (f_{SAW}, B_0) values that maximize the SWs attenuation length. The results are shown in the orange curve in Figure 7.d for the higher amplitude mode. Interestingly, we see that the attenuation length decreases for B_0 values greater than 34 mT. The shape of the signal for $B_0 < 29$ mT does not allow a good fit and the extraction of these quantities.

Analyzing Figures 7.b,d reveals that the ideal excitation configuration for the system is around the static field of 34 mT, where the contrast is of the order of a factor of 10, while the attenuation length of the SW is of the order of 1.6 μm.

Finally, we have studied the *influence of pad size on the generated spin wave*. We swept L_{pad} between 200 nm and 16 μm. Figures 8.a,b,c show the results obtained for the 3

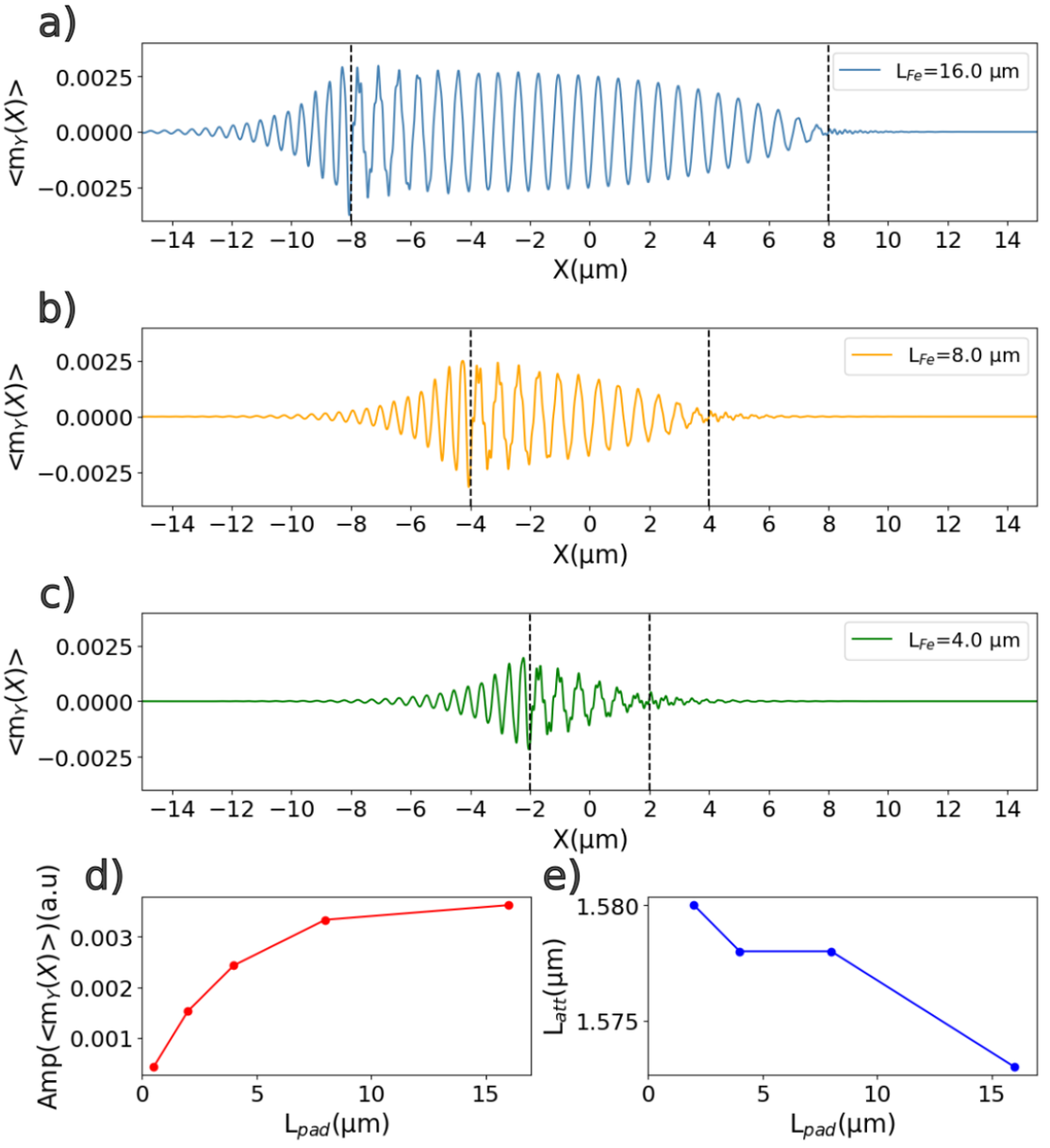

FIG. 8. (Color online). Profile of the transverse magnetization $\langle m_Y(X, 100 \times T)\rangle$ in the conduit at B_0 = 34 mT, f_{SAW} = 4.3 GHz and k_{SAW} = 9.46 rad/μm for a) L_{pad} = 16 μm, b) L_{pad} = 8 μm and c) L_{pad} = 4 μm. In each case, the edges of the Fe pad are shown by the black dashed lines. Spin wave amplitude (d) and attenuation length (e) as a function of pad size.

sizes L_{pad} = 16, 8 and 4 μm respectively, with B_2(FeN) = 1.8 MJ/m^3. Similar results (not shown) were obtained for the smallest pads. It is seen that both attenuation length L_{att} (Figure 8.e) and wave vector (not shown in the figure) do not depend on the pad size, proving that it is indeed the same mode that is excited, regardless of the pad size. On the other hand, the pad size clearly affects the amplitude of the signal, see Figure 8.d. The amplitude increases proportionally with the pad size up to L_{pad} = 2 μm, then increases more slowly until it seems to reach a limit beyond 16 μm. This result can be understood by considering the Fe pad as an antenna. The amplitude of the SWs generated in the FeN conduit being given by the coupling between the excitation in the antenna, here the asymmetric profile of the magnetization in the pad following the application of the SAW, and the profile of the SW eigenmode in the FeN conduit. Figures 8.a,b,c show that the asymmetric profile in the Fe pad requires several μm to develop and to reach his maximum amplitude around X = -$L_{pad}/2$, starting in general from zero around X = +$L_{pad}/2$. So, one solution to improve signal amplitude is to go for longer pad sizes, but Figure 8.d shows that beyond 6 μm, the gain becomes marginal. For example, between pads of lengths 4 and 16 μm, the gain

in signal amplitude is only a factor of 1.5, despite a factor of 4 on the pad size.

VII. DISCUSSION AND CONCLUSION

In conclusion, we have studied the generation of SWs in an FeN conduit from the excitation of an Fe pad at its centre with SAWs, using micromagnetic simulations magnetic paramaters for Fe and FeN. When the conduit and the pad are saturated, the working point where the SW is of maximum amplitude is trivial and is just the intersection between the dispersion curves of the Fe conduit and SAW. When the Fe pad is not saturated, there are several points of intersection and a study as a function of the SAW frequency is needed to deduce this point. Whatever the case, there is propagation of two SW modes in the conduit in agreement with the FeN dispersion curve. The largest amplitude mode has an attenuation length of the order of 1.6 μm. For this mode, which has the smallest wave vector, the amplitude is about a factor of 10 greater for the part of the wave propagating to the left (opposite to SAW propagation direction) of the pad than for the part propagating to its right (in the SAW propagation direction). A particular value of the magnetoelastic constant B_2 has been identified, for which the FeN conduit is insensitive to SAW, that allowed us to distinguish the authentic SW excitation from the Fe pad, isolating it from the magnetization dynamics induced by the SAW in the FeN conduit. Using this value in a detailed study of the response of the conduit to SAW excitation at different magnetic fields and frequencies, we highlighted the optimal working conditions for the system, namely around 34 mT, just above the Fe pad saturation field. At this point, the contrast between the SW generated in the conduit by the pad and the direct excitation of the conduit by the SAW is high, while having a high attenuation length. Finally, we emphasize that, compared to traditional inductive antenna-based SW generation[27], SAWs enable the excitation of monochromatic plane waves with a single propagation direction in the backward configuration. This unique characteristic results in the asymmetric SW generation demonstrated in this study. Looking ahead, we believe that integrating the real Rayleigh wave profile into the MuMax3 code, while accounting for strain and rotational terms, will enable a comprehensive understanding and precise engineering of SAW-assisted SW injection and propagation in SWs-conduits.

ACKNOWLEDGMENTS

This research was supported by the French ANR-22-CE24-0015 SACOUMAD. The authors would like to acknowledge the High Performance Computing Center of the University of Strasbourg for supporting this work by providing scientific support and access to computing resources. Part of the computing resources were funded by the Equipex Equip@Meso project (Programme Investissements d'Avenir) and the CPER Alsacalcul/Big Data. L. C., P. R., A. A and M. M. acknowledge support from the European Union within the HORIZON-CL4-2021-DIGITAL-EMERGING-01. Authors thank Laura Thevenard, Catherine Gourdon and Florian Millo for useful discussions and feedback on the manuscript.

AUTHOR DECLARATIONS

The authors have no conflicts to disclose.

DATA AVAILABILITY STATEMENT

The data that support the findings of this study are available from the corresponding author upon reasonable request.

Appendix A: Magnetic parameters of Fe and FeN

These parameters are shown in the Tables II and III.

TABLE II. Magnetic parameters of Fe.

Gyromagnetic factor	$\gamma = 184.7$ rad GHz.T^{-1}
Saturation Magnetization	$M_S = 1700$ kA.m^{-1}
Exchange coupling	$A_{ex} = 20$ pJ.m^{-1}
Cubic anisotropy	$K_{c1} = 49.6$ kJ.m^{-3}
Out-of-plane uniaxial anisotropy	$K_u = 100$ kJ.m^{-3}
Magnetoelastic constant	$B_2 = 7$ MJ.m^{-3}
Damping	$\alpha = 0.005$

TABLE III. Magnetic parameters of FeN.

Gyromagnetic factor	$\gamma = 184.7$ rad GHz.T^{-1}
Saturation Magnetization	$M_S = 1700$ kA.m^{-1}
Exchange coupling	$A_{ex} = 20$ pJ.m^{-1}
Cubic anisotropy	$K_{c1} = 40$ kJ.m^{-3}
Out-of-plane uniaxial anisotropy	$K_u = 150$ kJ.m^{-3}
Magnetoelastic constant	$B_2 = 7$ MJ.m^{-3}
Damping	$\alpha = 0.007$

Appendix B: Influence of SAW direction

This influence is shown in Figure 9. The blue curve in Figure 9.a corresponds to the blue curve in Figure 3.b, with the SAW and magnetic field oriented along the X-axis (from negative X to positive X). Keeping the same orientation of the magnetic field and reversing the direction of SAW propagation, we obtain the red curve in Figure 9.a. The blue curve is shown in Figure 9.b, while the central symmetry of the red curve, -$m_Y(-X)$, is shown instead.

We can see that the two curves coincide, which means that reversing the direction of SAW propagation results in an inversion of the signal by central symmetry with respect to the center of the conduit.

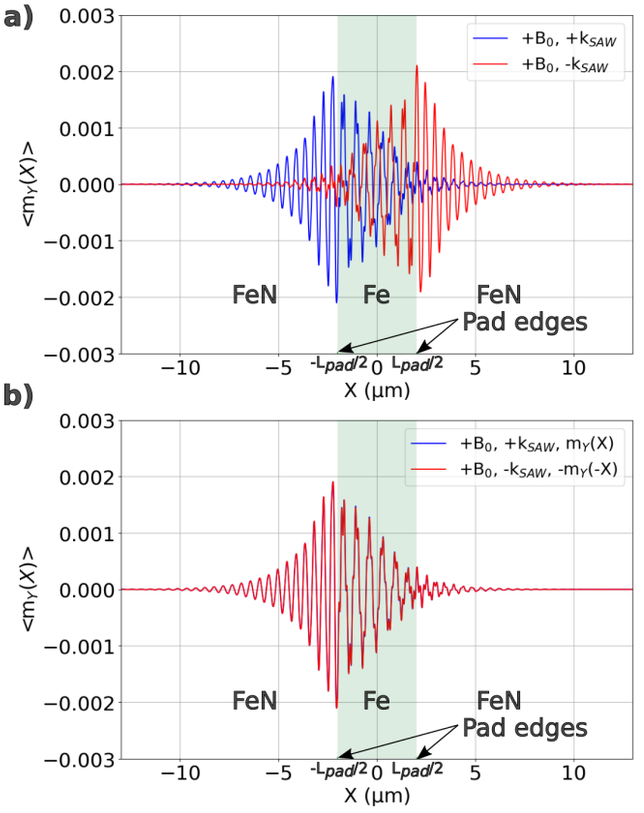

FIG. 9. (Color online). a) Profile of the transverse magnetization $\langle m_Y(X, 100\times T)\rangle$ within the conduit at f_{SAW} = 4.32 GHz, B_0 = 34 mT and k_{SAW} = 9.46 rad/μm (blue curve) and k_{SAW} = - 9.46 rad/μm (red curve). b) Comparison of the 2 signals : the change in SAW direction (the sign of k_{SAW}) leads to a signal inversion (by central symmetry with respect to the center of the waveguide). A positive (negative) sign of B_0 or k_{SAW} means an orientation of the magnetic field or SAW wave vector from negative (positive) X to positive (negative) X. In a) and b), the region of the Fe pad is shown with the green transparent rectangle. The pad edges are also indicated.

Appendix C: Magnetoelastic field - Change of reference frame

(xyz) is the standard cubic frame and (XYZ) is the rotated frame in which the conduit is defined in the simulation, see Figure 10. The rotation matrix from (XYZ) to (xyz) is :

$$R = \begin{pmatrix} c & -s & 0 \\ s & c & 0 \\ 0 & 0 & 1 \end{pmatrix} \tag{C1}$$

with $c = \cos(45°) = \sqrt{2}/2$ and $s = \sin(45°) = \sqrt{2}/2$. The relations between the magnetization components and the strain tensor components between the two reference frames are given by $\boldsymbol{m}' = R^T\boldsymbol{m}$ and $\varepsilon' = R^T\varepsilon R$ where R^T is the transpose of R and $\boldsymbol{m} = \begin{pmatrix} m_X \\ m_Y \\ m_Z \end{pmatrix}$, $\boldsymbol{m}' = \begin{pmatrix} m_x \\ m_y \\ m_z \end{pmatrix}$. In the case where the SAW is assumed to be a plane wave deformation of the form

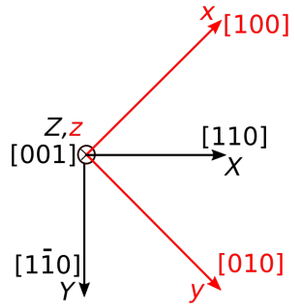

FIG. 10. (Color online). Representation of the the standard cubic (xyz) and the frame (XYZ), rotated by 45° with respect to (xyz).

$\boldsymbol{u}(X,t) = (u_{0X}\cos(k_{SAW}X - \omega t),\ 0,\ u_{0Z}\sin(k_{SAW}X - \omega t))$, one finds :

$$\begin{cases} \varepsilon_{XX} = \frac{\partial u_X}{\partial X}, \varepsilon_{YY} = 0, \varepsilon_{ZZ} = 0 \\ \varepsilon_{XY} = 0, \varepsilon_{YZ} = 0, \varepsilon_{XZ} = \frac{1}{2}\frac{\partial u_Z}{\partial X} \end{cases} \tag{C2}$$

$$\begin{cases} \varepsilon_{xx} = \frac{1}{2}\varepsilon_{XX}, \varepsilon_{yy} = \frac{1}{2}\varepsilon_{XX}, \varepsilon_{zz} = 0 \\ \varepsilon_{xy} = -\frac{1}{2}\varepsilon_{XX}, \varepsilon_{yz} = -\frac{\sqrt{2}}{2}\varepsilon_{XZ}, \varepsilon_{xz} = \frac{\sqrt{2}}{2}\varepsilon_{XZ} \end{cases} \tag{C3}$$

By replacing the different terms with the appropriate expressions in equation 2, one finds :

$$\boldsymbol{H}^{ME}(X,Y,Z) = -\frac{2}{\mu_0 M_S}\begin{pmatrix} \frac{B_1+B_2}{2}m_X\varepsilon_{XX} + B_2 m_Z\varepsilon_{XZ} \\ \frac{B_1-B_2}{2}m_Y\varepsilon_{XX} \\ B_2 m_X\varepsilon_{XZ} \end{pmatrix} \tag{C4}$$

The relations between the components of the rotation tensor between the two reference frames are given by $\omega' = R^T\omega R$ where $\omega_{ij} = \frac{1}{2}\left(\frac{\partial u_i}{\partial X_j} - \frac{\partial u_j}{\partial X_i}\right)$ with $i, j = X, Y, Z$. With the SAW $\boldsymbol{u}(X,t) = (u_{0X}\cos(k_{SAW}X - \omega t),\ 0,\ u_{0Z}\sin(k_{SAW}X - \omega t))$, we get ω_{xz} = -$\sqrt{2}/2\ \varepsilon_{XZ}$, $\omega_{yz} = \sqrt{2}/2\ \varepsilon_{XZ}$ and ω_{XZ} = -ε_{XZ} so that one deduces from equation 5 :

$$\boldsymbol{H}^{MR}(X,Y,Z) = M_s\varepsilon_{XZ}\begin{pmatrix} m_Z \\ 0 \\ m_X \end{pmatrix} \tag{C5}$$

.

Finally, one obtains the total effective field given by the equation 6 by adding the two expressions in the above equations C4 and C5.

Appendix D: SW characteristics

Figure 11 shows fits of SW profiles generated in the FeN conduit from the Fe pad, at different f_{SAW} around f_{SAW} = 4.32 GHz, at B_0 = 34 mT.

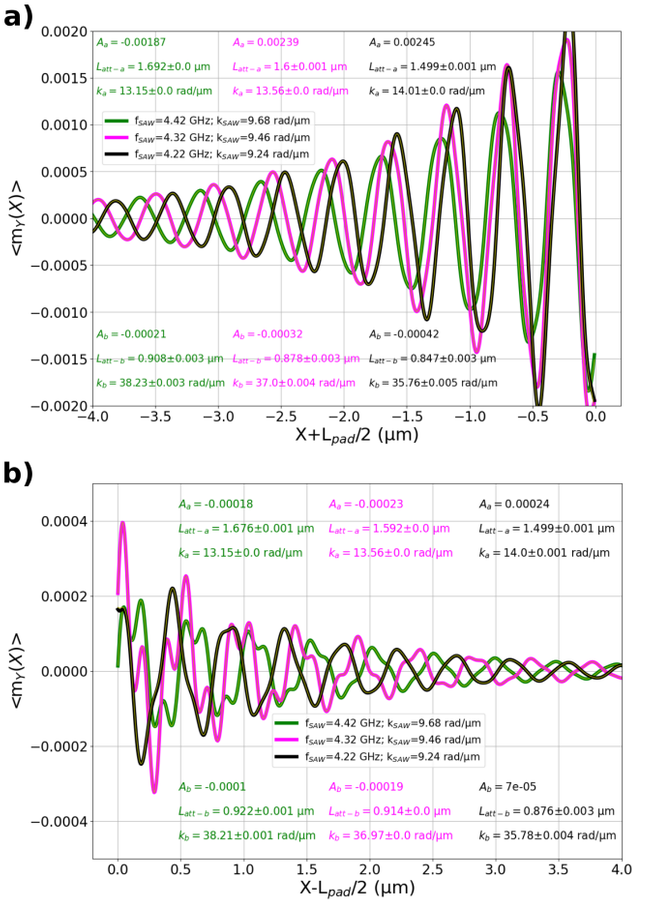

FIG. 11. (Color online). Fits of spin wave profiles generated in the FeN conduit from the Fe pad, at different f_{SAW} around f_{SAW} = 4.32 GHz, at B_0 = 34 mT. For each frequency, the part of the signal to the left of the pad ($X < -L_{pad}/2$) is shown in a), while the part to the right ($X > L_{pad}/2$) is shown in b). For each case, the fit curve is shown in thinner yellow line.

[1] V. V. Kruglyak, S. O. Demokritov, and D. Grundler, en"Magnonics," Journal of Physics D: Applied Physics **43**, 264001 (2010).
[2] A. V. Chumak, V. Vasyuchka, A. Serga, and B. Hillebrands, en"Magnon spintronics," Nature Physics **11**, 453–461 (2015).
[3] A. Barman, G. Gubbiotti, S. Ladak, A. O. Adeyeye, M. Krawczyk, J. Gräfe, C. Adelmann, S. Cotofana, A. Naeemi, V. I. Vasyuchka, B. Hillebrands, S. A. Nikitov, H. Yu, D. Grundler, A. V. Sadovnikov, A. A. Grachev, S. E. Sheshukova, J.-Y. Duquesne, M. Marangolo, G. Csaba, W. Porod, V. E. Demidov, S. Urazhdin, S. O. Demokritov, E. Albisetti, D. Petti, R. Bertacco, H. Schultheiss, V. V. Kruglyak, V. D. Poimanov, S. Sahoo, J. Sinha, H. Yang, M. Münzenberg, T. Moriyama, S. Mizukami, P. Landeros, R. A. Gallardo, G. Carlotti, J.-V. Kim, R. L. Stamps, R. E. Camley, B. Rana, Y. Otani, W. Yu, T. Yu, G. E. W. Bauer, C. Back, G. S. Uhrig, O. V. Dobrovolskiy, B. Budinska, H. Qin, S. van Dijken, A. V. Chumak, A. Khitun, D. E. Nikonov, I. A. Young, B. W. Zingsem, and M. Winklhofer, en"The 2021 Magnonics Roadmap," Journal of Physics: Condensed Matter **33**, 413001 (2021).
[4] A. V. Chumak, A. A. Serga, and B. Hillebrands, "Magnon transistor for all-magnon data processing," Nature Communications **5** (2014), 10.1038/ncomms5700.
[5] G. Talmelli, T. Devolder, N. Träger, J. Förster, S. Wintz, M. Weigand, H. Stoll, M. Heyns, G. Schütz, I. P. Radu, J. Gräfe, F. Ciubotaru, and C. Adelmann, "Reconfigurable submicrometer spin-wave majority gate with electrical transducers," Science Advances **6**, eabb4042 (2020), https://www.science.org/doi/pdf/10.1126/sciadv.abb4042.
[6] M. Evelt, V. E. Demidov, V. Bessonov, S. O. Demokritov, J. L. Prieto, M. Muñoz, J. B. Youssef, V. V. Naletov, G. de Loubens, O. Klein, M. Collet, K. Garcia-Hernandez, P. Bortolotti, V. Cros, and A. Anane, "High-efficiency control of spin-wave propagation in ultra-thin yttrium iron garnet by the spin-orbit torque," Applied Physics Letters **108**, 172406 (2016).
[7] M. Grassi, M. Geilen, D. Louis, M. Mohseni, T. Brächer, M. Hehn, D. Stoeffler, M. Bailleul, P. Pirro, and Y. Henry, "Slow-wave-based nanomagnonic diode," Phys. Rev. Appl. **14**, 024047 (2020).
[8] A. GANGULY, K. DAVIS, D. WEBB, and C. VITTORIA, "Magnetoelastic surface-waves in a magnetic film piezoelectric substrate configuration," JOURNAL OF APPLIED PHYSICS **47**, 2696–2704 (1976).
[9] M. Weiler, L. Dreher, C. Heeg, H. Huebl, R. Gross, M. S. Brandt, and S. T. B. Goennenwein, "Elastically driven ferromagnetic resonance in nickel thin films," PHYSICAL REVIEW LETTERS **106** (2011), 10.1103/PhysRevLett.106.117601.
[10] L. Thevenard, C. Gourdon, J. Y. Prieur, H. J. von Bardeleben, S. Vincent, L. Becerra, L. Largeau, and J. Y. Duquesne, "Surface-acoustic-wave-driven ferromagnetic resonance in (ga,mn)(as,p) epilayers," PHYSICAL REVIEW B **90** (2014), 10.1103/PhysRevB.90.094401.
[11] P. Delsing, A. N. Cleland, M. J. A. Schuetz, J. Knoerzer, G. Giedke, J. I. Cirac, K. Srinivasan, M. Wu, K. C. Balram, C. Bauerle, T. Meunier, C. J. B. Ford, P. V. Santos, E. Cerda-Mendez, H. Wang, H. J. Krenner, E. D. S. Nysten, M. Weiss, G. R. Nash, L. Thevenard, C. Gourdon, P. Rovillain, M. Marangolo, J.-Y. Duquesne, G. Fischerauer, W. Ruile, A. Reiner, B. Paschke, D. Denysenko, D. Volkmer, A. Wixforth, H. Bruus, M. Wiklund, J. Reboud, J. M. Cooper, Y. Fu, M. S. Brugger, F. Rehfeldt, and C. Westerhausen, "The 2019 surface acoustic waves roadmap," JOURNAL OF PHYSICS D-APPLIED PHYSICS **52** (2019), 10.1088/1361-6463/ab1b04.
[12] J. Puebla, Y. Hwang, S. Maekawa, and Y. Otani, "Perspectives on spintronics with surface acoustic waves," APPLIED PHYSICS LETTERS **120** (2022), 10.1063/5.0093654.
[13] P. G. Gowtham, T. Moriyama, D. C. Ralph, and R. A. Buhrman, "Traveling surface spin-wave resonance spectroscopy using surface acoustic waves," Journal of Applied Physics **118**, 233910 (2015), https://pubs.aip.org/aip/jap/article-pdf/doi/10.1063/1.4938390/15171587/233910_1_online.pdf.
[14] Y. Kunz, M. Kuess, M. Schneider, M. Geilen, P. Pirro, M. Albrecht, and M. Weiler, "Coherent surface acoustic wave-spin wave interactions detected by micro-focused brillouin light scattering spectroscopy," APPLIED PHYSICS LETTERS **124** (2024), 10.1063/5.0189324.
[15] M. Xu, K. Yamamoto, J. Puebla, K. Baumgaertl, B. Rana, K. Miura, H. Takahashi, D. Grundler, S. Maekawa, and Y. Otani, "Nonreciprocal surface acoustic wave propagation via magneto-rotation coupling," Science Advances **6**, eabb1724 (2020), https://www.science.org/doi/pdf/10.1126/sciadv.abb1724.
[16] S. Maekawa and M. Tachiki, "Surface acoustic attenuation due to surface spin wave in ferro- and antiferromagnets," AIP Conference Proceedings **29**, 542–543 (1976), https://pubs.aip.org/aip/acp/article-pdf/29/1/542/11729027/542_1_online.pdf.
[17] T. Amarouche, L.-C. Garnier, M. Marangolo, M. Eddrief, V. H. Etgens, F. Fortuna, Y. Sadaoui, M. Tamine, J. L. Cantin, and H. J. von Bardeleben, "Influence of ion implantation parameters on the perpendicular magnetic anisotropy of fe-n thin films with stripe domains," Journal of Applied Physics **121**, 243903 (2017).
[18] L.-C. Garnier, *Couches minces en Fe-N élaborées par implantation ionique : propriétés structurales et magnétiques*, Theses, Université Paris Saclay (COmUE) (2019).
[19] P. Rovillain, J.-Y. Duquesne, L. Christienne, M. Eddrief, M. G. Pini, A. Rettori, S. Tacchi, and M. Marangolo, "Impact of spin-wave dispersion on surface-acoustic-wave velocity," Phys. Rev. Appl. **18**, 064043 (2022).
[20] A. Vansteenkiste, J. Leliaert, M. Dvornik, M. Helsen, F. Garcia-Sanchez, and B. V. Waeyenberge, "The design and verification of MuMax3," AIP Advances **4**, 107133 (2014).
[21] D. ROYER and E. Dieulesaint, en*Elastic Waves in Solids I: Free and Guided Propagation* (Springer Science & Business Media, 1999) google-Books-ID: SzwQ1UYspyQC.

[22]J.-Y. Duquesne, P. Rovillain, C. Hepburn, M. Eddrief, P. Atkinson, A. Anane, R. Ranchal, and M. Marangolo, "Surface-acoustic-wave induced ferromagnetic resonance in fe thin films and magnetic field sensing," Phys. Rev. Appl. **12**, 024042 (2019).

[23]This approximation is valid when $\partial u_X/\partial Z$ is neglected, and $\partial u_Z/\partial X$ is treated as a constant. This can be the case when the Fe/GaAs system is covered by a high-velocity thin layer. For example, for a 20 nm diamond layer, one finds that $\partial u_Z/\partial X$ is almost constant while the ratio between $\partial u_Z/\partial X$ and $\partial u_X/\partial Z$ is about a factor of 2. It would be interesting to find stratagies to achieve this goal, where we would have about a factor 10 between $\partial u_Z/\partial X$ and $\partial u_X/\partial Z$.

[24]K. Yamamoto, M. Xu, J. Puebla, Y. Otani, and S. Maekawa, "Interaction between surface acoustic waves and spin waves in a ferromagnetic thin film," Journal of Magnetism and Magnetic Materials **545**, 168672 (2022).

[25]Y. Hwang, J. Puebla, K. Kondou, C. Gonzalez-Ballestero, H. Isshiki, C. S. Muñoz, L. Liao, F. Chen, W. Luo, S. Maekawa, and Y. Otani, "Strongly coupled spin waves and surface acoustic waves at room temperature," Phys. Rev. Lett. **132**, 056704 (2024).

[26]A. V. Chumak, A. A. Serga, and B. Hillebrands, "Magnonic crystals for data processing," Journal of Physics D: Applied Physics **50**, 244001 (2017).

[27]T. Devolder, "Propagating-spin-wave spectroscopy using inductive antennas: Conditions for unidirectional energy flow," Phys. Rev. Appl. **20**, 054057 (2023).